
Article:
Aslam, A., Morley, N.A. orcid.org/0000-0002-7284-7978, Amin, N. et al. (8 more authors) (2021) Study of structural, optical and electrical properties of La3+ doped Mg0.25 Ni0.15 Cu0.25 Co0.35 Fe2-x Lax O4 spinel ferrites. Physica B: Condensed Matter, 602. 412565. ISSN 0921-4526

https://doi.org/10.1016/j.physb.2020.412565

Study of structural, optical and electrical properties of La^{3+}doped $Mg_{0.25}$ $Ni_{0.15}$ $Cu_{0.25}$ $Co_{0.35}$ Fe_{2-x} La_x O_4 spinel ferrites

Asma Aslam[a], N. A. Morley[b], Nasir Amin[a], Muhammad Imran Arshad[a]*, Muhammad Ajaz un Nabi[a], Adnan Ali[a], Khalid Mahmood[a], Aisha Bibi[c], Faisal Iqbal[d], Sajad Hussain[e], Yasir Jamil[f],

[a]*Department of Physics, Government College University, Faisalabad, Pakistan.*
[b]*Department of Materials Science and Engineering, The University of Sheffield, UK, S1 3JD.*
[c]*Institute of Functional Nano & Soft Materials (FUNSOM), Soochow University, Suzhou, Jiangsu 215123, China.*
[d]*Department of Physics, The Islamia University of Bahawalpur, Pakistan.*
[e]*Department of Physics, Division of Science and Technology, University of Education, Lahore, Pakistan.*
[f]*Department of Physics, University of Agriculture Faisalabad, Pakistan.*

*Corresponding Author: miarshadgcuf@gmail.com

Abstract

Lanthanum substituted Mg-Ni-Cu-Co ferrite nanoparticles prepared through the Sol-Gel method were studied using different methods such as XRD, FTIR, UV-VIS, SEM, Raman, LCR, EDX and IV to evaluate the structural, optical and electrical properties. The single-phase cubic spinel structure of the prepared samples was confirmed from X-ray diffraction analysis. The FT-IR spectra indicated two absorption bands, ν_1 and ν_2 that represent the complex Fe^{3+}–O^{2-} at A- site (tetrahedral) and B-site (octahedral) vibration. The optical band gap decreased from 2.48eV to 1.53eV observed by UV-Vis, and matched with the electrical resistivity measurements. Variation in the lattice parameters from XRD, the absorption band (octahedral) from FTIR, the optical energy band gap from the UV-vis data and the DC resistivity demonstrated change in structural, optical and electric properties of Mg-Ni-Cu-Co ferrites nanoparticles due to the addition of the rare earth element La^{3+}. Both the dielectric losses and dielectric constant of the prepared samples decreased due to the La^{3+} ions doping, and A.C conductivity increased with increasing the value of frequency from 8 Hz to 8M Hz. The variation in Raman peaks reveals that Raman shift varied due to the La^{3+} addition. EDX data confirmed the stoichiometric calculations of La^{3+}ions substituted into Mg-Ni-Cu-Co ferrite nanoparticles.

Keywords: Ferrites; doping; Single-phase; Raman; Resistivity;

Introduction:

Nanostructured materials are a rapidly growing research field within academic institutes, laboratories and industries. Nanomaterials can be found in fused, single and aggregated procedures with irregular, tubular and spherical forms. The mostly commonly used nanomaterials consist of dendrimers, nanotubes, fullerenes and quantum dots [1, 2]. In recent years, the nano ferrites spinel compounds have been investigated for their uses in technology fields for example high density information storage, drug delivery, magnetic chips and ferro fluids etc. The importance of doped rare earth ions have increased, as they change the structure and texture of nano ferrites spinel compounds [3, 4].The multi- functional properties and potential applications of nano ferrites spinel compounds have found use in microwave, computer technology, actuators and transducers etc. [5]. The enhanced magnetic, electrical and optical properties of spinel ferrites have various benefits e.g. they are less expensive, have reliable stability, easy preparation and having different magnetic properties compared to other types of nanomaterials. The ion distribution splits the spinel ferrites into two categories, which are normal spinel structure and inverse spinel structure. The chemical formula for inverse spinel structure is A $[B_2]$ O_4 where A is divalent and B is trivalent cation and occupies tetrahedral and octahedral sites respectively. Heat treatment and their chemical composition effect the distributions of these particles either on the octahedral (B) or tetrahedral (A) sites [6]. Lanthanum is of interest to dope in these nanoferrites as the simple electronic spectrum of Lanthanum prefers its use for experiential analysis because at its fusion point it has the lowest vapor pressure and the highest boiling point.

Ahmed et al. [7] explained the effect of doping of La^{3+} on magnesium ferrites in which La^{3+} ions replaced Fe^{3+} at octahedral site that cause the formation of orthoferrite phase at certain condition of the prepared samples. As a result, the electric and magnetic properties of La^{3+} doped ferrites changed due to interaction of Fe-Fe. The value of resistivity for the dopant La^{3+} (x=0.025) was approximately 1.21×10^{6} Ωcm at 505 K due to absence of ‘‘4f’’ orbital that slow down the conduction as well as polarization.

Khanna et al. [8] reported rare earth element La^{3+} doped copper nanoparticles synthesized by the sonochemical technique. The reported research work revealed the value of A.C conductivity of La^{3+} (x=0.15) doped sample is 1.28×10^{-4} $\Omega^{-1}cm^{-1}$ while its value is 6.96×10^{-4} $\Omega^{-1}cm^{-1}$ without

La^{3+} (x=0) doping that showed A.C conductivity decreased with the addition of La^{3+} ions at room temperature.

Bharathi et al. [9] prepared rare earth element La^{3+} doped Co ferrite nanoparticles through solid-state chemical reaction technique. As a result, the electric properties of La^{3+} doped Co nanoparticles exponentially decreased with decrease in temperature and the value of electric conductivity at 300 K is 0.623×10^{-8} $\Omega^{-1}cm^{-1}$.

P. Kumar et al. [10] revealed the effect of La^{3+} doping on the magnetic, dielectric and electric properties of $CoFe_2O_4$ ferrites synthesized by co-precipitation technique. This research reported that DC resistivity of prepared cobalt nanoparticles at room temperature is 6.465×10^{5} Ωcm without doping of La^{3+} while its value for x=0.15 of La^{3+} doping is 26.990×10^{6} Ωcm.

R. Indhrajothi et al. [11] prepared cobalt ferrite nanoparticles with the addition of La^{3+} through glycerol assisted foam combustion technique that enhanced the capacity retention and oxidation reaction of Fe and Co of the prepared samples. The value of A.C conductivity is 1.75×10^{-6} $\Omega^{-1}cm^{-1}$ in the absence of La^{3+} while its value is 2.18×10^{-8} $\Omega^{-1}cm^{-1}$ with the addition of La^{3+}(x= 0.06) measured at 303 K. The doping of La^{3+} ions in the prepared nanoparticles reduced the electrical conductivity of cobalt ferrite due to slow down electron hopping. Slimani et al. [12] reported Eu^{3+} doped Ni-Cu-Zn ferrite through sonochemical approach that decrease the reaction time and reduce the requirement of large quantity of organic solvents. A.C conductivity of Eu^{3+} doped Ni-Cu-Zn SPNs varied and it is minimum for x = 0.02 at 393 K. Almessiere et al. [13] prepared Co-Zn nanoparticles through hydrothermally with the addition of three different doped metals as Ce, Dy and Y. It observed from XRD data that lattice constant 'a' decreased due to doping of rare earth elements.

Almessiere et al. [14] reported $Ni_{0.3}Cu_{0.3}Zn_{0.4}Fe_2O_4$ NSFs prepared through ultrasonic irradiation technique. The maximum variation of conductivity was observed for x=0.02 at 350 K while the maximum conductivity find out for x=0.03.

Almessiere et al. [15] prepared Dy^{3+} substituted $Mn_{0.5}Zn_{0.5}Fe_{2-x}O_4$ nanoparticles through the ultrasonic irradiation technique in which the doping of Dy in prepared samples decreased the band energy gap calculated from Tauc equation from 1.67 eV to 1.61 eV.

Sadaqat et al. [16] synthesized Tb^{3+} doped Co nanoparticles implemented sonochemical technique in which the lattice constant of prepared samples reduced from x=0.00 to x=0.04 due to doping of Tb^{3+}.

There are several techniques the preparation of the soft spinel ferrites such as solid state reaction [17], co-precipitation [18], reverse micelle technique [19] and auto combustion sol-gel techniques [20]. Among all those techniques, sol-gel auto-combustion is considered the most appropriate and useful technique [21].

In present work of research, we synthesized La^{3+} doped series of $Mg_{0.25}$ $Ni_{0.15}$ $Cu_{0.25}$ $Co_{0.35}$ Fe_{2-x} La_xO_4 spinel ferrites where x varies as 0, 0.03, 0.06, 0.09, 0.12 and 0.15 through auto combustion sol gel method. The effects of La^{3+} ions on optical, electrical and structural parameters of prepared spinel ferrites are discussed in this article.

2. Experimental Details

2.1. Materials and synthesis

The series of $Mg_{0.25}$ $Ni_{0.15}$ $Cu_{0.25}$ $Co_{0.35}$ Fe_{2-x} La_x $O_4$where x varies as 0.00, 0.03, 0.06, 0.09, 0.12, 0.15 was prepared through the method of sol-gel-auto-combustion. The following chemicals [$Mg(NO_3)_2.6H_2O$], [$Ni(NO_3)_2•6H_2O$], [$Cu(NO_3)_2•3H_2O$], [$Co(NO_3)_2.6H_2O$], [$Fe(NO_3)_3.9H_2O$] and [$La(NO_3)_3.6H_2O$] were dissolved in distilled water according to their stoichiometry calculations, in a beaker on a magnetic stirrer with continuous stirring. Citric acid [$C_6H_8O_7•H_2O$] was taken according to the stoichiometry calculation and dissolved in a separate beaker with continuously stirring on a magnetic stirrer. After obtaining a homogeneous solution of all the metal nitrates, the citric acid solution was added into the solution containing all the chemicals and mixed well. To attain a pH=7 for the solution, the ammonia was added into it. After maintaining the pH, the heat was turn up to 80˚C, so that the gel was formed and then turn into ash that sintered at 800°C for 8 h. The obtained powder after grinding was converted into pellets of diameter 7mm using a hydraulic press.

2.2 Characterization Techniques

The structure of all the prepared samples was characterized using different techniques. The XRD technique with CuK_α source of wavelength 1.5406Å investigated the cubic spinel structure of the prepared samples. All the structural parameters such as lattice constant, theoretical density, experimental density, d-spacing, packing fraction, strain, porosity, x-ray density, bulk density, dislocation density and crystallite size were determined through the XRD technique. The electrical resistivity was measured by the two probe IV measurement techniques and the optical parameters were measured by UV-VIS spectroscopy, to find the energy band gap. The cation

distribution at interstitial A-site and B-sites were determined by FTIR Spectroscopy. The SEM data revealed the morphological characteristics of the synthesized nanoparticles and the EDX technique confirmed the stoichiometric amount of all samples. Raman analysis was used to confirm the substitution of La^{3+} into the nano-ferrites. A LCR meter was used to determine the dielectric losses in the frequency range from 8 HZ to 8 MHz due to La^{3+} ions doping. The activation energy and electrical resistivity trends were calculated from the two probes IV technique data.

3. Results and Discussion

3.1. Structural studies

XRD analysis of$Mg_{0.25}Ni_{0.15}Cu_{0.25}Co_{0.35}Fe_{2-x}La_xO_4$ where x = 0.00, 0.03, 0.06, 0.09, 0.12 and 0.15 samples is shown in Fig.1. It shows diffraction peaks at (220), (311), (400), (422) and (511) which confirmed the existence of spinel structure of the prepared samples due to doping of La^{3+} ions. The peak corresponding to $2\theta = 32.21^{o}$ is due to traces of the secondary phase $LaFeO_3$ at the boundaries of the specimen, as it is not cubic spinel phase peak [22]. It is observed that the $LaFeO_3$ diffraction peak intensity increases with the increase of La^{3+} ions doping. The secondary phase presence of La^{3+} ions in Mg-Ni-Cu-Co-La ferrites evaluates the limit of solubility of La^{3+}substitution in the cubic lattice of spinel ferrites [23, 24].

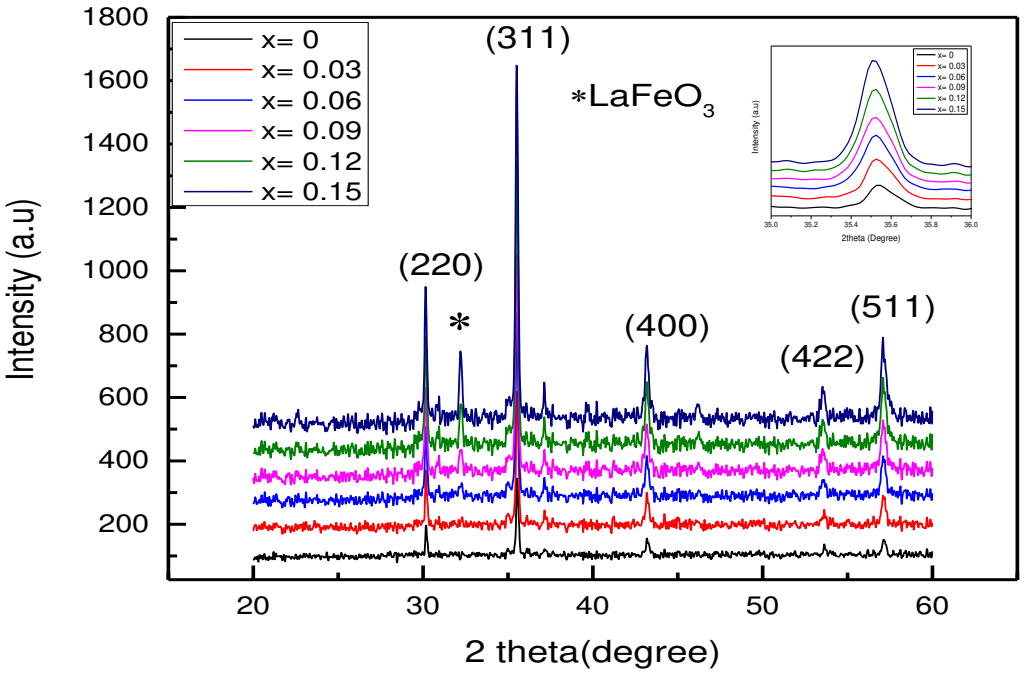

Fig.1. Powder XRD data of $Mg_{0.25}Ni_{0.15}Cu_{0.25}Co_{0.35}Fe_{2-x}La_x$ O_4spinel ferrites sintered at 800°C for 8 hours.

Fig.1 shows that the highest peak (311) becomes narrow and an extra peak which is actually La^{3+} peak is observed at 32.21°due to the increase in La^{3+} concentration from x= 0 to 0.15. The formula of Bragg's law is used to evaluate the inter planer distance and its formula is given below

$$d = n\lambda / 2\sin\theta \qquad (1)$$

Here 'n' is the positive integer which represents the reflections order and taken to equal to one while 'λ' represents the wavelength that is 1.5406Å and 'θ' indicates the angle of Bragg's law.

The lattice constants for the synthesized particles were calculated by the following formula

$$a= d*(h^2 + k^2 + l^2)^{1/2} \qquad (2)$$

Here, 'a' represents lattice constant, 'd' indicates inter planer distance while hkl represent Miller indices [25].

For calculations of the crystalline size, Scherrer's formula was used which is given below

$$D = \frac{n\lambda}{\beta Cos\theta} \qquad (3)$$

Here ‘D’ is the crystalline size, ‘λ’ represents wavelength taken in nm (0.15418 nm), ‘β’ indicates the Full width at half maxima (FWHM) and θ reveals the angle Bragg’s law and n= 0.94 represents crystalline shape factor [26].

Table.1. lattice parameter, interplant distance, crystallite size and theoretical x-ray density of $Mg_{0.25}Ni_{0.15}Cu_{0.25}Co_{0.35}Fe_{2-x}La_xO_4$.

Samples	Lattice constants	Interplane Distance	Crystallite Size	X-ray density
	a (Å)	d (Å)	D (nm)	ρ_x(g/cm^3)
x= 0.00	8.362	2.5212	51.081	5.1587
x= 0.03	8.367	2.5228	46.785	5.2054
x= 0.06	8.375	2.5251	41.693	5.2477
x= 0.09	8.371	2.5241	41.084	5.310
x= 0.12	8.372	2.5240	50.533	5.3757
x= 0.15	8.370	2.5243	51.703	5.4395

The calculated values of crystallite size, interplane distance and lattice parameter of intense peak at (311) are listed in table 1.

It was observed from Table.1 that the value of lattice constant increased from x= 0 to x= 0.06 due to La^{3+} deposited on the grain boundaries as an impurity and not diffused into the crystal lattice. But with increasing the concentration La^{3+} doping, the La^{3+} started to diffuse into the crystal lattice and the value of lattice constant increased. The ionic radii of La^{3+} is 1.05 Å which inclines toward octahedral B-site because Fe^{3+} particles (ionic radii = 0.67 Å) involved three various types of destinations [27]. The replacement of a few Fe^{3+} particles from the tetrahedral to octahedral sites demonstrated variation in crystal lattice and crystalline size due to doping of La^{3+} in the prepared samples [28].

The theoretical value of x-ray density $\rho_x$increases as the La^{3+} concentration increases in the prepared samples and it was calculated through the following formula. .

$$\rho_x = \frac{8M}{N_A a^3} \qquad (4)$$

Here N_A represents the Avogadro's number ($6.022 \times 10^{23} mol^{-1}$), M indicates molecular weight of the prepared samples.

Accurate value of ‘a’ were confirmed through Nelson- Riley function F (θ) by using the technique of least square fit and its formula is given as

$$F(\theta) = \frac{1}{2}\left[\frac{Cos^2\theta}{\text{Sin}\theta} + \frac{Cos^2\theta}{\theta}\right] \quad (5)$$

F (θ) calculated values given in table 2 are well matched with the experimental calculated values of 'a'.

The value of F (θ) increased from x= 0 to 0.06 and then decreased from x = 0.09 to 0.15 by increasing the concentration of doped La^{3+} due to larger ionic radii of La^{3+}(1.05 Å) compared to the iron radii (0.645 Å).

$$\rho_{bulk} = \frac{Mass}{Volume} = \frac{M}{\pi r^2 \times h} \quad (6)$$

Here h indicates thickness of the pellet while the radius of the pellet is represented by r. It was observed from the calculation that the bulk density depended on the mass of the pellet.

The given relation used to find out the porosity of the samples

$$P\% = \left[1 - \frac{\rho_b}{\rho_x}\right] \times 100 \quad (7)$$

Here, the bulk density indicated by $\rho_b$while X-ray density represented by $\rho_x$as mentioned in Table.1. It reveals an increasing trend in the values of $\rho_x$while the values of ρ_b showed variation that is due to presence of some inevitable pores produced during the process of sintering and synthesis of the samples[29]. The variation in the calculated values of the bulk density is due to the doping of La^{3+}that have larger atomic weight (amu) compared to Fe^{2+}(amu) which also resulted in a decline trend in porosity.

The porosity has nonlinear trend for La^{3+} concentration as x varies from 0.00 to 0.15.

Therefore, different parameters such as packing factor (p), the specific surface area (S) and strain (ε) from the XRD data were calculated from the formulas in equations (8), (9) and (10) respectively and presented in table 2.

$$P = \frac{D}{d} \quad (8) \qquad S = \frac{6000}{\rho_x \times D} \quad (9)$$

$$\varepsilon = \frac{1}{d^2} \quad (10)$$

Here the crystalline size is represented by D while inter planar distance is indicated by d. [30, 31].

Table.2. F (**θ**), ρ_b, P ,S, p and ε of $Mg_{0.25}$ $Ni_{0.15}$ $Cu_{0.25}$ $Co_{0.35}$ Fe_{2-x} La_x O_4

Samples	**F(θ)**	**Bulk Density**	**Porosity**	**Specific surface Area**	**Packing Factor**	**Strain**
x	Rad	ρ_b(g/cm^3)	(P %)	S (m^2/g)	p(%)	(ε)
0	2.9451	2.933	43.144	40.047	20.261	0.1573
0.03	2.9474	2.948	43.366	43.503	18.545	0.1571
0.06	2.9506	2.9634	43.529	48.562	16.511	0.1568
0.09	2.9492	2.9788	43.902	49.071	16.276	0.1569
0.12	2.9491	2.9634	44.874	40.067	20.021	0.1570
0.15	2.9402	2.9483	45.881	39.361	20.482	0.1569

Cation Distribution

The ionic radii r_A(Å) and r_B(Å) were calculated using the mathematical expressions in equations (11) and (12) respectively and represents the cation distribution of tetrahedral and octahedral sites for the prepared samples in table 4 [32]. The cationic radii of Mg, Ni, Co, Cu, La, and Fe respectively are listed in table 3.

$$r_A = C_{AMg}r(Mg^{2+}) + C_{ANi}r(Ni^{2+}) + C_{ACu}r(Cu^{2+}) + C_{ACo}r(Co^{2+}) + C_{AFe}r(Fe^{2+}) \quad (11)$$

$$r_B = \frac{1}{2}[C_{BMg}r(Mg^{2+}) + C_{BCo}r(Co^{2+}) + C_{BCu}r(Cu^{2+}) + C_{BNi}r(Ni^{2+}) + C_{BLa}r(La^{3+}) + C_{BFe}r(Fe^{2+})] \quad (12)$$

Table.3. The cationic radii of Mg, Ni, Co, Cu, La, and Fe respectively of series $Mg_{0.25}Ni_{0.15}Cu_{0.25}Co_{0.35}Fe_{2-x}La_xO_4$

Elements	A-site (%)	B-site (%)	r_A (Å)	r_B(Å)	References
Mg	5	95	0.57	0.72	[33]
La	0	100	-	1.05	[22]
Ni	10	90	0.69	0.78	[22]
Cu	15	85	0.57	0.73	[34]
Co	20	80	0.58	0.74	[35]
Fe	-	-	0.60	0.645	-

Table 4: Cationic distribution estimated for $Mg_{0.25}Ni_{0.15}Cu_{0.25}Co_{0.35}Fe_{2-x}La_xO_4$ using XRD analysis

x	Tetrahedral site	Octahedral site
0	$[Mg_{0.0125}Ni_{0.015}Co_{0.07}Cu_{0.0375}Fe_{0.865}]_A$	$[Mg_{0.2375}Ni_{0.135}Co_{0.28}Cu_{0.2125}La_0Fe_{1.135}]_BO_4$
0.03	$[Mg_{0.0125}Ni_{0.015}Co_{0.07}Cu_{0.0375}Fe_{0.865}]_A$	$[Mg_{0.2375}Ni_{0.135}Co_{0.28}Cu_{0.2125}La_{0.03}Fe_{1.105}]_BO_4$
0.06	$[Mg_{0.0125}Ni_{0.015}Co_{0.07}Cu_{0.0375}Fe_{0.865}]_A$	$[Mg_{0.2375}Ni_{0.135}Co_{0.28}Cu_{0.2125}La_{0.06}Fe_{1.075}]_BO_4$
0.09	$[Mg_{0.0125}Ni_{0.015}Co_{0.07}Cu_{0.0375}Fe_{0.865}]_A$	$[Mg_{0.2375}Ni_{0.135}Co_{0.28}Cu_{0.2125}La_{0.09}Fe_{1.045}]_BO_4$
0.12	$[Mg_{0.0125}Ni_{0.015}Co_{0.07}Cu_{0.0375}Fe_{0.865}]_A$	$[Mg_{0.2375}Ni_{0.135}Co_{0.28}Cu_{0.2125}La_{0.12}Fe_{1.015}]_BO_4$
0.15	$[Mg_{0.0125}Ni_{0.015}Co_{0.07}Cu_{0.0375}Fe_{0.865}]_A$	$[Mg_{0.2375}Ni_{0.135}Co_{0.28}Cu_{0.2125}La_{0.15}Fe_{0.985}]_BO_4$

Table 5 shows that the ionic radii r_A(Å) remains constant due to no addition of La^{3+} ion onto the tetrahedral site while r_B(Å) increased due to the doping of La^{3+} ions (1.05 Å) which are larger than the Fe^{3+} ions (0.645 Å) they replace.

a_{th} represents the theoretical lattice constant and is given in Equation (13)[36].

$$a_{th}= \frac{8}{\sqrt[3]{3}}[(r_A + R_o) + \sqrt{3} (r_B + R_o)] \qquad (13)$$

Here, the ionic radii of samples at tetrahedral and octahedral sites are represented by r_A, and r_B respectively while R_o indicates the oxygen ion radius that is equal to 1.32 Å.

The calculated values of a_{th} values are given in Table.5 and show that the calculated values of theoretical lattice constant (a_{th}) increased due to the doping of La^{3+} ions.

The calculated tolerance factor (T) is given in equation (14) [37].

$$T= \frac{1}{\sqrt{3}}\left(\frac{rA + Ro}{rB + Ro}\right) + \frac{1}{\sqrt{2}}\left(\frac{Ro}{rA + Ro}\right) \qquad (14)$$

The spinel structure of the prepared samples is confirmed with the help of the tolerance factor (T) when it is equal to one. The slightly difference from one in the values of T shows the effect of La^{3+} ions doping into the prepared samples.

Relation (15) is used to find out the oxygen positional parameter (U) [38].

$$U = (r_A + R_o)\frac{1}{\sqrt{3}a} + \frac{1}{4} \qquad (15)$$

It is confirmed from reported literature that the standard value of oxygen positional parameter is 0.375 Å and the variation in U represent the slightly difference of obtained spinel structure of the prepared samples from ideal spinel structure due to the displacement of the anion from the ideal structure of spinel ferrites [39]. Table.5 represents the variation of values of oxygen positional parameter due to doping of La^{3+} ions concentration into the prepared samples of ferrites.

Table 5: The various x-ray parameters of for $Mg_{0.25}Ni_{0.15}Cu_{0.25}Co_{0.35}Fe_{2-x}La_xO_4$ using XRD analysis

composition (x)	r_A(Å)	r_B(Å)	a_{th}(Å)	u(Å)	T
0	0.5984	0.6854	8.3013	0.3825	1.0388
0.03	0.5984	0.6914	8.3173	0.3824	1.0372
0.06	0.5984	0.6975	8.3336	0.3823	1.0355
0.09	0.5984	0.7036	8.3498	0.38231	1.0338
0.12	0.5984	0.7097	8.3658	0.38232	1.0322
0.15	0.5984	0.7157	8.3821	0.38233	1.03061

3.2. FTIR

The prepared samples of Lanthanum doped soft ferrites were investigated using FT-IR analysis. The FT-IR analysis explains the cation distribution at tetrahedral and octahedral sites in ferrites materials. FTIR spectra presented in Fig. 2 show two major frequency bands where v_1 represents the higher frequency band while v_2 represents the lower frequency band. The variation in the intrinsic vibrations of the B- site (octahedral) of the prepared samples show that La^{3+} ions prefer the octahedral site due to having a larger ionic radius (1.05 Å) than Fe^{3+} (0.645 Å). This has an impact on the stretching vibration of $Fe^{3+}\_O^{2-}$ which changes the position of the bands. A slight variation in the stretching band frequency v_2 is clear from table.6 that confirms the preference of La^{3+} ions existence on the octahedral sites [40].

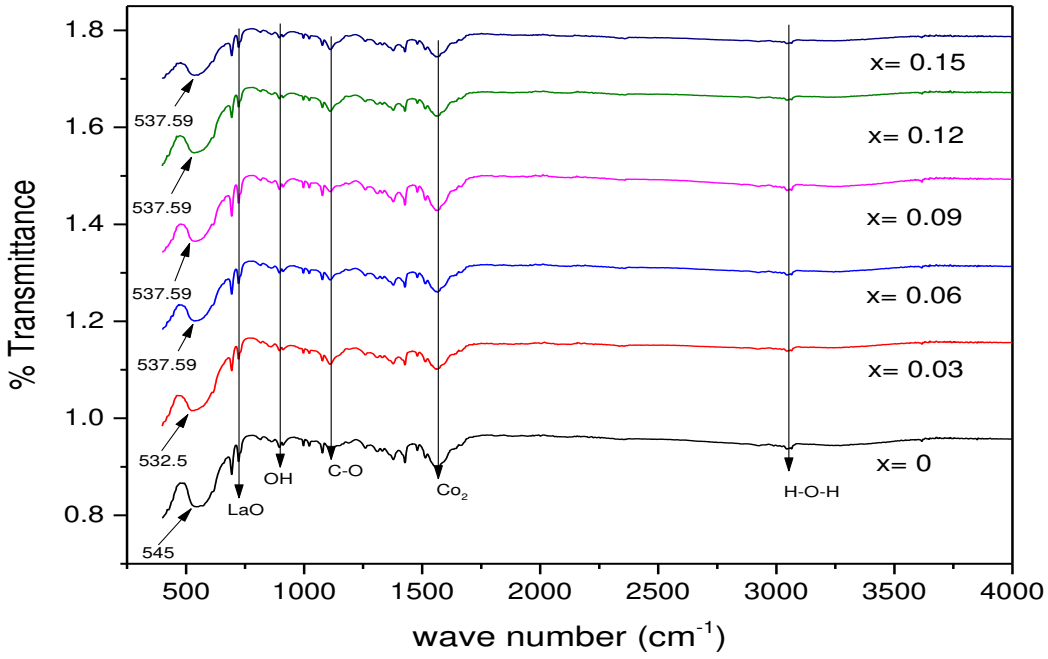

Fig.2: FTIR spectrum of $Mg_{0.25}Ni_{0.15}Cu_{0.25}Co_{0.35}Fe_{2-x}La_xO_4$spinel ferrites

The force constant was calculated for the ions at the octahedral and tetrahedral sites and is given in equation (16) [41].

$$K = 4\pi^2 c^2 v^2 \mu \qquad (16)$$

Where K represents force constant, c indicates the velocity of light, v represents the vibration frequency while here the reduced mass is represented by μ (2.601×10^{-23} g).

Krysewski et al. [42] described that deformation of the iron oxide lattice peak at 883 cm^{-1} due to the bonding of Fe_3O_4 particles with surface OH groups. The stretchable vibration of the H–O–H group may provide an absorption peak due to the presence of residual water in the range from 1630 cm^{-1} to 3420 cm^{-1} in FT-IR data [43]. The peak that appeared at 1120 cm^{-1} may be due to the remaining C–O bond vibration [44]. The appearance of the significant peak at 1432 cm^{-1} is due to presence of carbonate ion [45]. The FTIR spectrum reveals a peak at 1000 cm^{-1} that is reported in literature due to the incomplete decomposition of the products and two prominent peaks appeared at 795 cm^{-1} (La-O) and 1316 cm^{-1} (C-O) reveals the existence of the oxalate ion while in this research work these peaks appeared at 729 cm^{-1} and 1378 cm^{-1} respectively [46]. The significant peak appearance at 1584 cm^{-1} reported in this work is due to the presence of CO_2

anti-symmetrical vibration [47] while in the present research work it is appeared at 1568 cm^{-1} in the prepared samples due to doping of La^{3+}.

Table 6: The various parameters of for $Mg_{0.25}Ni_{0.15}Cu_{0.25}Co_{0.35}Fe_{2-x}La_xO_4$ using FTIR and UV-Vis analysis

X	**V_1 (cm^{-1})**	**Force constant (dyne/cm)**	**V_2 (cm^{-1})**	**Force constant (dyne/cm)**	**Optical band gap (Eg) (eV)**
0	545.38	275099.97426	425.44	167405.13465	2.48
0.03	532.5	262259.57845	425.04	167090.49299	2.13
0.06	537.59	267297.25434	423.72	166054.27538	1.94
0.09	537.59	267297.25434	420.416	163474.72155	1.78
0.12	537.59	267297.25434	424.16	166399.32313	1.67
0.15	537.59	267297.25434	423.23	165670.43913	1.53

3.3 Optical properties

The solution of La^{3+} doped $Mg_{0.25}Ni_{0.15}Cu_{0.25}Co_{0.35}Fe_{2-x}La_xO_4$ where x varies as 0.00, 0.03, 0.06, 0.09, 0.12, 0.15 ferrite nanoparticles were prepared by using de-ionized water as a solvent to obtain the UV- vis spectra. The ultraviolet or visible region of light provide energy to non-bounding electrons in the absorption of UV-vis spectroscopy then these electrons interacted with the orbits of anti-bonding molecules in an excitation mode.

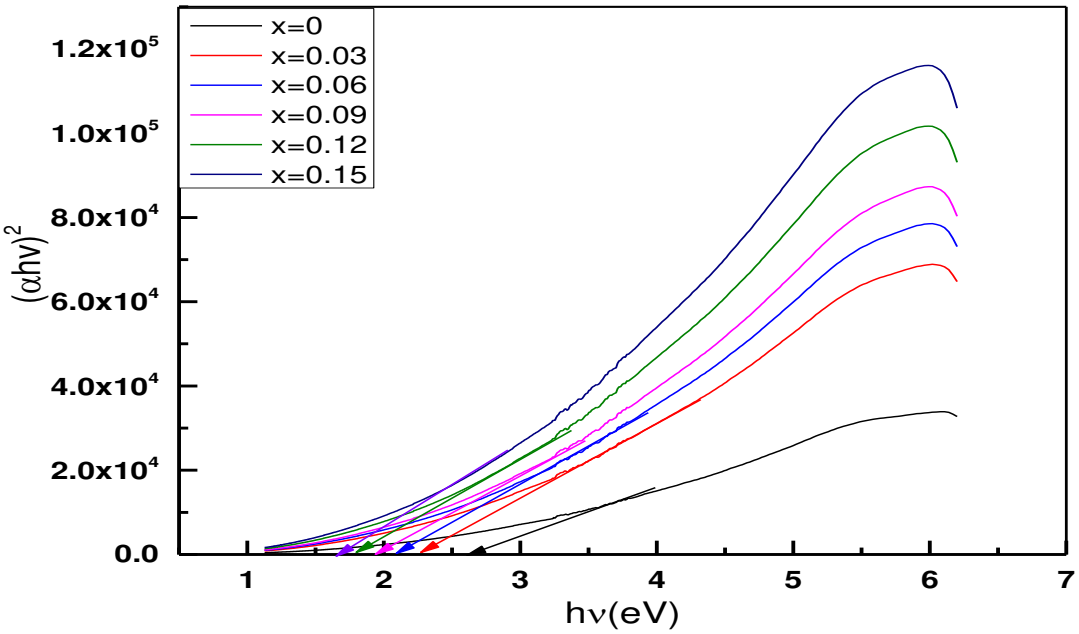

Fig. 3: Absorption Spectrum of UV-Vis with band gap energy (E_g) for $Mg_{0.25}Ni_{0.15}Cu_{0.25}Co_{0.35}Fe_{2-x}La_xO_4$

Equation (17) is known as Tauc's relation and is used to find out the band energy gap of UV- Vis absorption Spectrum.

$$\alpha h\nu = B(h\nu - Eg)^m \qquad (17)$$

Here $h\nu$ represents the photons energy that strikes the samples and B is a constant while m is a dependent constant that varies with the gap between the conduction and valance band that may be ½ or 2. The formula for the calculation of absorption coefficient α is given below as,

$$\alpha = 2.303\frac{\log(A)}{t} \qquad (18)$$

Here '$\boldsymbol{\alpha}$' represent absorbance and t = 1cm indicates breadth of material. The graph between $(\alpha h\nu)^2$ and $(h\nu)$ evaluates the energy band gap due to doping of La^{3+} ions in the samples.

Fig. 3 reveals that there is a decrease in energy band gap due to La^{3+} ions doping in the prepared nanoparticles. The energy band gap is 2.48 eV for the sample without La^{3+} doping. The energy band gap significantly decreased and was found to be 1.53 eV for x= 0.15 due to La^{3+} doping in the prepared samples as mentioned in Table.6 that is matched with reported literature [48, 49].

Therefore, the doping of larger ionic radii of La^{3+} (1.05 Å) reduced the band energy gap and also varied the lattice constant of the crystal lattice. The basic reason of the reduction in the band energy gap is the loose bonding of electrons with the nucleus that reveal less amount of energy is needed to remove electron from the outermost shell due to addition of La^{3+} ions [50].

3.4. Raman

If a Raman mode is contained more than one type of cations in which the resulting peak is one of containing of involvement from different cations in the same symmetry. These peaks are reasonably de-convoluted and each sub peak coordinated force proportional to the relating cations of unit cell. Therefore, five peaks of Raman data are found in the range of 150- 750 cm^{-1} as shown in figure 4. The first mode A_{1g}represents the symmetric stretching of the bond exist between (Fe/M)-O while its anti- symmetric stretching represented by T_{2g} (2) mode. T_{2g}(3) represents the anti-symmetric and E_g indicates the anti-symmetric abasement methods of oxygen concerning Fe- O bond. The translational development of MO_4 (tetrahedron) is represented byT_{2g} (1) that is the fifth mode of Raman spectroscopy [51]. These five modes of Raman data confirmed the spinel structure with a similar space gathering of samples with the addition of La^{3+}ions.

The cation distributions disturb in spinel ferrites due to doping of rare earth cations in unit cell that evaluate through an adjustment in position and power of Raman peaks in the form of bond length, steady power and electronegativity at octahedral and tetrahedral of the vibrating species [52].

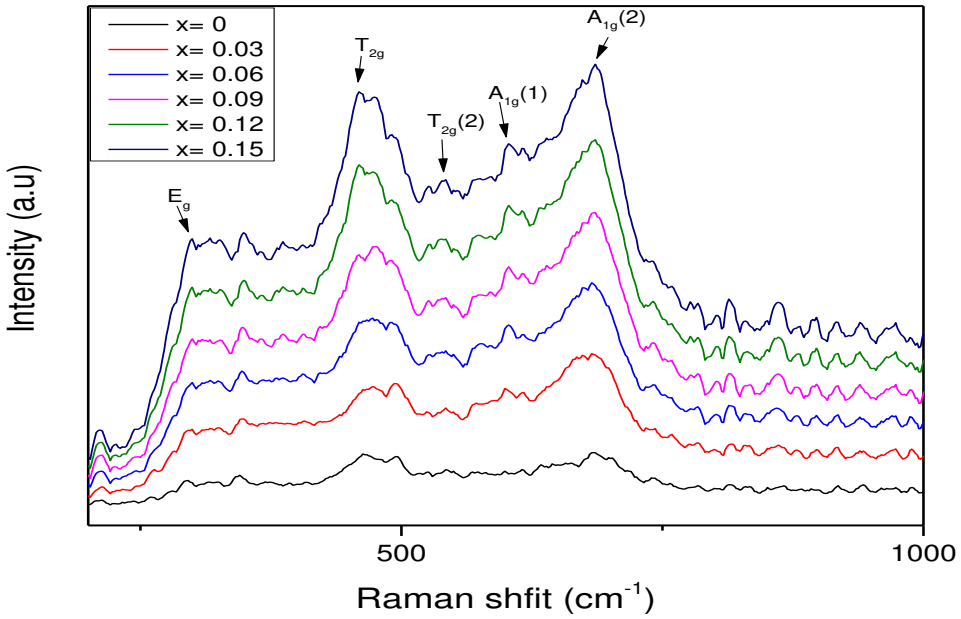

Fig.4: The five modes of lanthanum doped $Mg_{0.25}Ni_{0.15}Cu_{0.25}Co_{0.35}Fe_{2-x}La_xO_4$ where x varies as 0.00, 0.03, 0.06, 0.09, 0.12, 0.15 ferrites has range E_g 298 to 305cm^{-1}, $T_{2g}(2)$ 460 to 469cm^{-1}, $T_{2g}(3)$ 533 to 545cm^{-1}, $A_1g(1)$ 600 to 603cm^{-1} and $A_{1g}(2)$ 683 to 686cm^{-1}.

For all sample's wavelengths are illustrated in table 7 given below

Table 7: Raman absorption peaks for different concentration of La^{3+}.

x	E_g (cm^{-1})	$T_{2g}(2)$ (cm^{-1})	$T_{2g}(3)$ (cm^{-1})	$A_{1g}(1)$ (cm^{-1})	$A_{1g}(2)$ (cm^{-1})
0.00	299	464	544	600	683
0.03	300	466	545	601	684
0.06	300	469	533	603	684
0.09	298	461	542	603	686
0.12	299	460	539	601	684

0.15	305	460	542	603	685

3.5. Dielectric analysis

The dielectric properties of La^{3+} doped series of $Mg_{0.25}$ $Ni_{0.15}Cu_{0.25}$ $Co_{0.35}Fe_{2-x}La_x$ $O_4$where x varies as 0, 0.03, 0.06, 0.09, 0.12, 0.15 were studies through the LCR technique that represented the incline or decline trend in the values of dielectric constant and A.C conductivity by varying the f (8Hz- 8M Hz).

3.5.1 Dielectric Constant

The relation between the dielectric constant (ε') with log (f) is given in Fig 5.

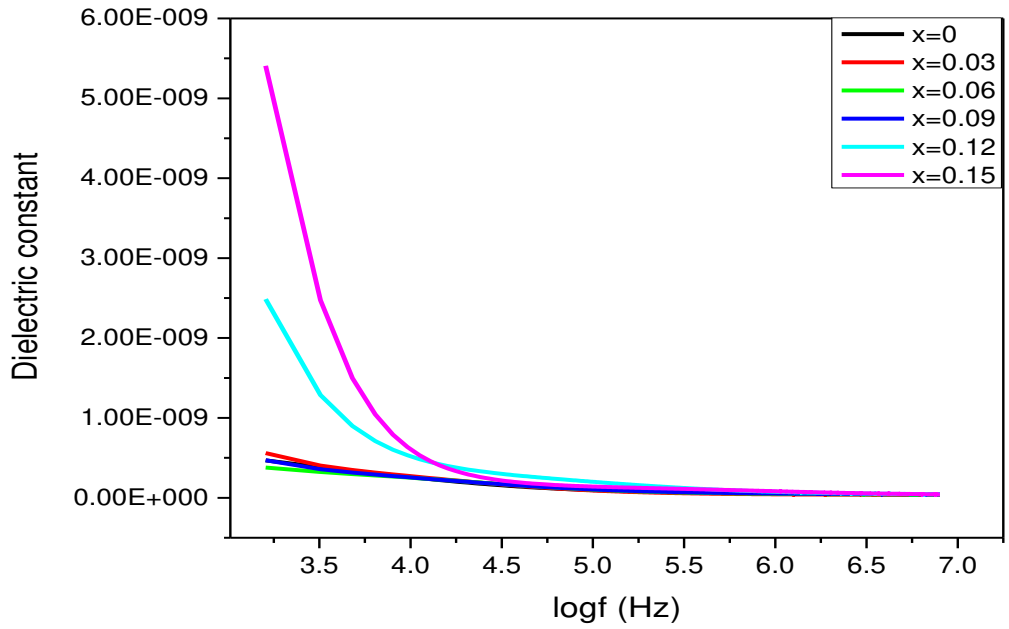

Fig.5: Graph between Dielectric constant and logf

This graph showed that there is a decreased in dielectric constant with the addition of La^{3+} ions. From these results, it is clear that increasing the La^{+3} concentrations the frequency has a decreasing trend. This change in the dielectric with frequency of soft magnetic ferrites is due to the synthetic techniques, the frequency of dielectric, temperature, stoichiometric and crystalline size of the prepared samples. Dielectric behavior is due to the hoping and polarization of charges

[53]. At lower frequency the hopping is easy and the dielectric constant has sharp values but as the frequency increases the hopping becomes difficult due to the alternating frequency so the dielectric value decreases. The other reason for the dielectric constant dispersion is due to the polarization of charges at the grain boundaries with the addition of La^{3+} ions doping [54].

3.5.2 Dielectric loss

The variation in dielectric loss with log(f) is as shown in Fig.6.

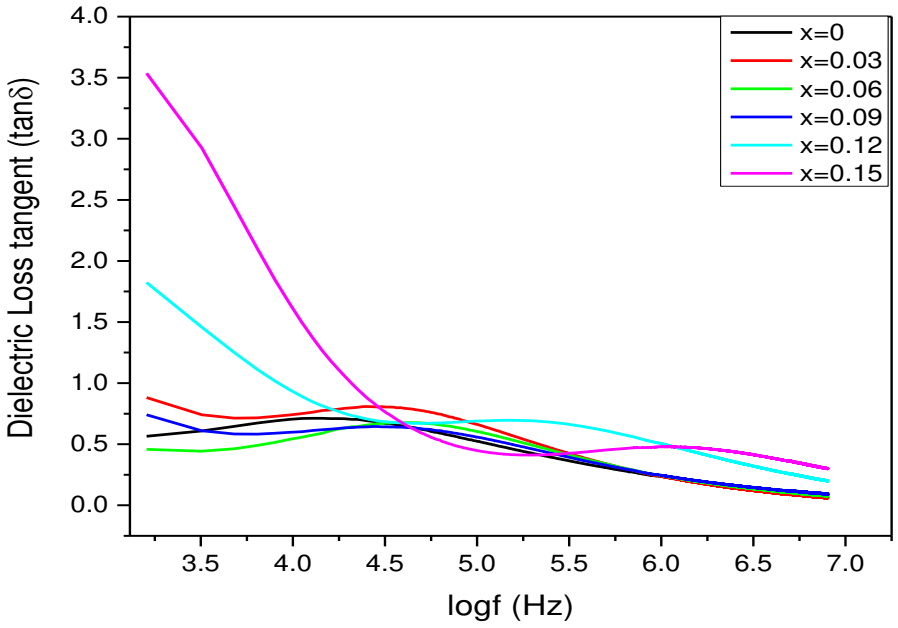

Fig.6. Graph between dielectric loss tangent and log(f)

Fig.6 shows the variation in dielectric loss tangent by changing the frequency from 8Hz to 8MHz, such that it decreased with the addition of La^{3+} ions. The dielectric loss decreased with increasing the frequency, which means there is an inverse relation between frequency and tanδ.

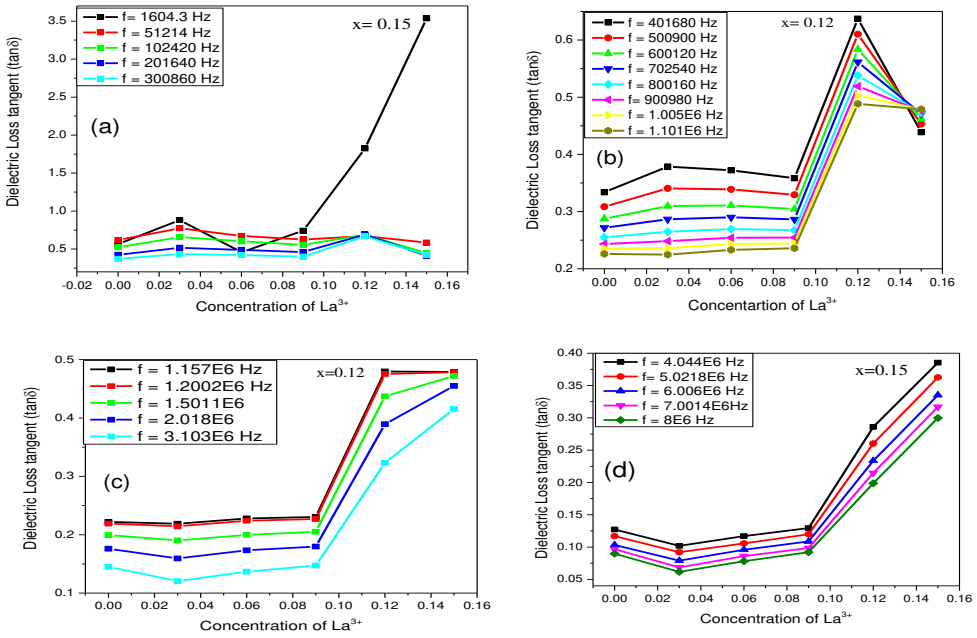

Fig.7. Graph between dielectric loss tangent and Concentration of La^{3+} at different frequencies

Fig.7(a) shows the trend of dielectric loss for the frequency range from 1604 Hz to 300860 Hz which has a maximum value of dielectric loss for x= 0.15 and has a minimum value for x=0.00.

Fig. 7(b) indicates that the dielectric loss is maximum for x= 0.12 and minimum for x=0.00 in the frequency range from 400,000 Hz to 1.101E6 Hz.

Fig. 7(c) reveals that the maximum and minimum value of dielectric value is observed for x=0.12 and x= 0.03 respectively at frequency range from 1.15E6 Hz to 3.103E6 Hz.

Fig. 7(d) showed the dielectric loss behavior which is maximum for x = 0.15 and minimum for x = 0.03 from frequency 4.044E6 Hz to 8E6 Hz.

Thus Fig. 7 demonstrates tangent loss decline trend as frequency increases. At lower frequencies the loss was high due to the hopping of electron following the applied field. After certain value of frequency the loss starts to decrease due to the hopping electrons not following the applied field.

3.5.3 Q-factor

The variation in Q-factor with log(f) is as shown in Fig.8.

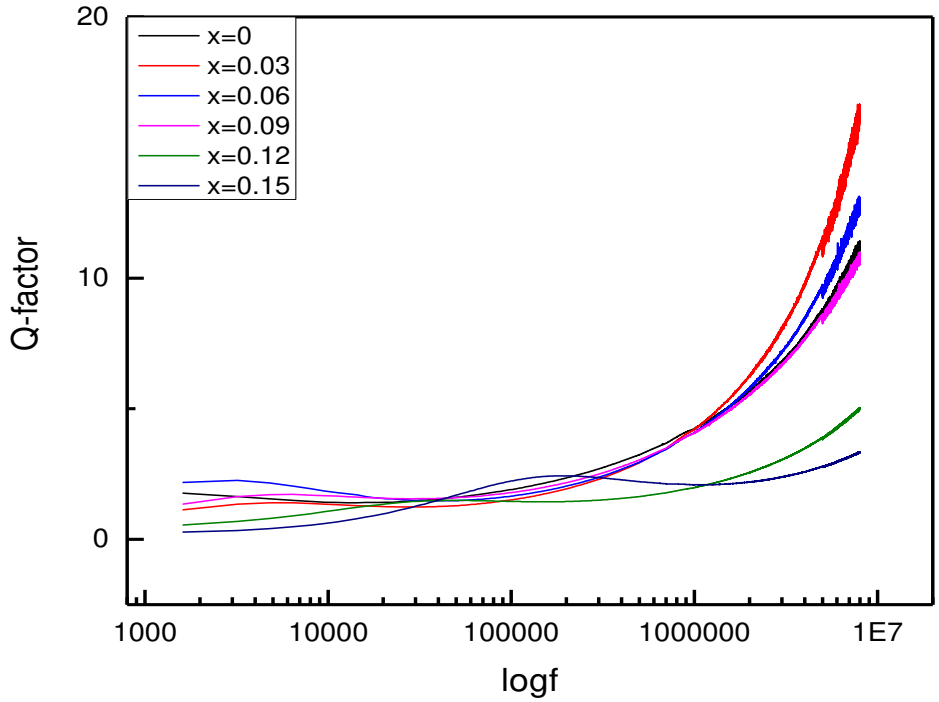

Fig.8. Graph between Q-factor with log(f)

This graph showed that the value of Q-factor increased by adding La^{3+}ions concentration in each sample such that varies as x from 0 to 0.15. The Q-factor provides the relation between stored energy and the rate of dissipation of energy in different electrical devices. For this reason, Q-factor values give useful information with frequency provide about the prepared La^{3+} doped samples and the nonlinear trend of Q-factor represents the typical behavior of ferrites as reported literature [55].

3.5.4 A. C Conductivity

The relation in equation (19) is used to find out the A. C conductivity of the prepared samples.

$$\sigma = \omega \varepsilon_r \varepsilon_0 \tan \delta \qquad (19)$$

Here, ω is the angular frequency that is equal to $2\pi f$, ε_r is the relative permittivity, ε_0 is the dielectric constant and $\tan\delta$ is tangent loss factor.

The variation in dielectric loss with log(f) is as shown in Fig.9.

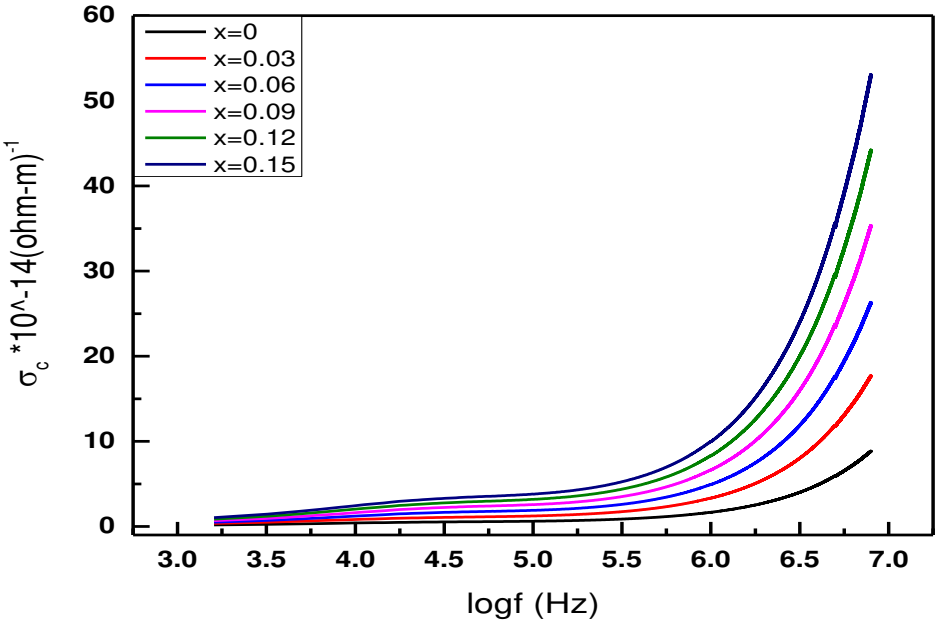

Fig.9. Graph between ac conductivity and log(f)

This graph showed that the value of A. C conductivity increased by adding La^{3+} ions to the ferrites. The increase in A.C conductivity represents the typical behavior of ferrites due to having highly conductive grain boundaries according to Koop's theory polarization that is good agreement with the reported literature [20, 56].

3.6. Scanning Electron Microscopy (SEM)

SEM micro images for $Mg_{0.25}Ni_{0.15}Cu_{0.25}Co_{0.35}Fe_{2-x}La_xO_4$ where x varies as 0.0, 0.03, 0.06, 0.09, 0.12 and 0.15 spinel ferrites in pellet form with 7mm diameter are shown in the Fig. 10 (a-f). The micrographs reveal most nanoparticles are smaller lower than 100 nm. The SEM data confirmed the difference in size between the doped and un-doped particle size. The doped nano-ferrites samples had more uniformity with the addition of Lanthanum which basically increased the

homogeneity of grain size. It is accomplished through the diffusion of La^{3+} ions near the grain boundaries that creates ion and oxygen vacancies and controls the boundary mobility [57, 58].

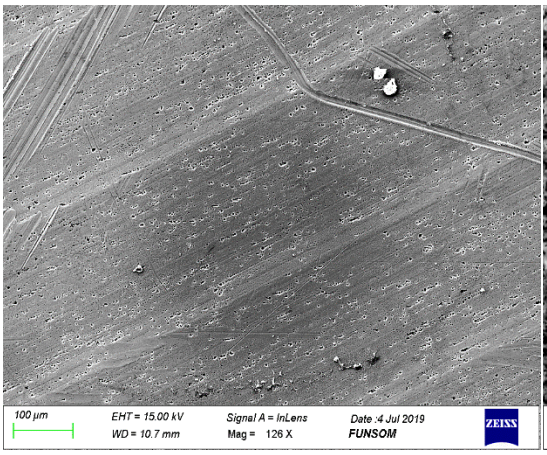

(a) For x=0

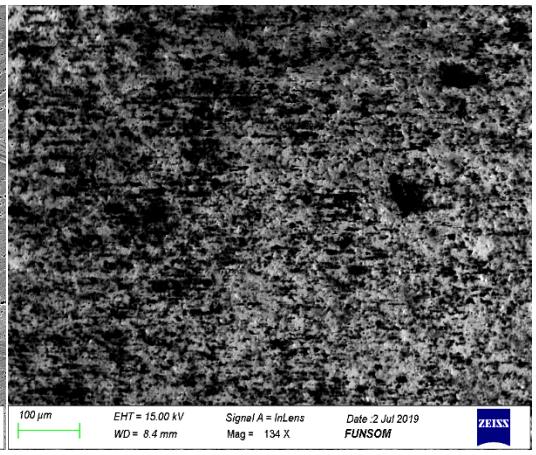

(b)For x=0.03

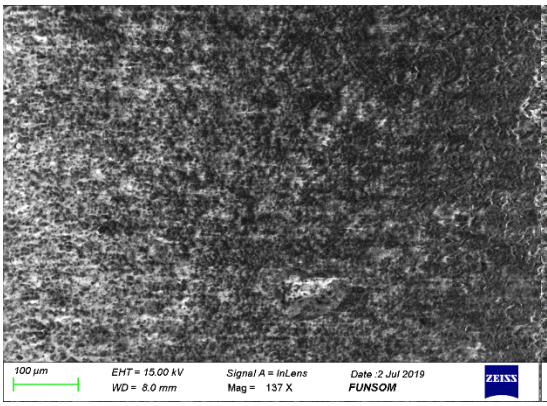

(c)For x=0.06

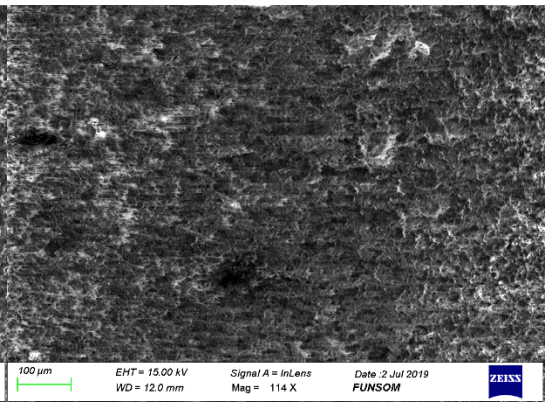

(d)For x=0.09

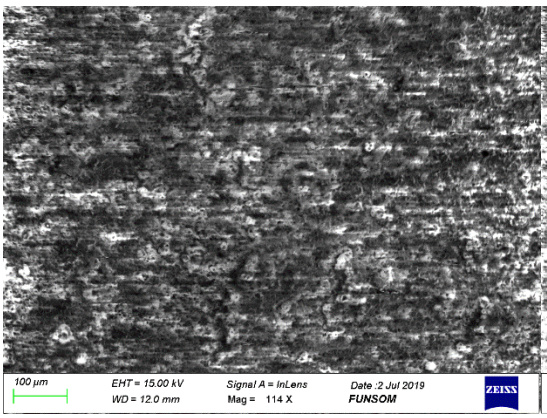

(e) For x=0.12

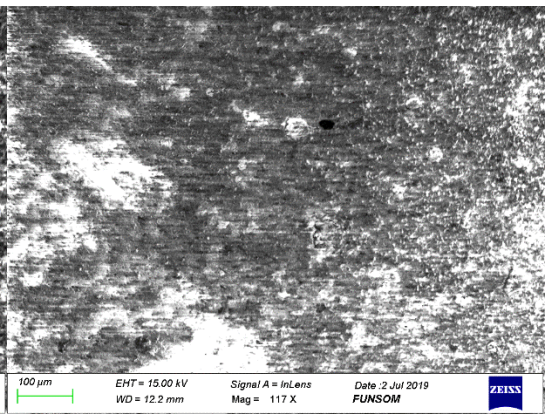

(f) For x=0.15

Fig. 10 (a-f): Images of SEM for $Mg_{0.25}Ni_{0.15}Cu_{0.25}Co_{0.35}Fe_{2-x}La_xO_4$ where x varies as 0.00, 0.03, 0.06, 0.09, 0.12, 0.15

3.7. Energy dispersive X-ray spectroscopy (EDS)

The scattering of X-ray spectroscopy called EDS was utilized to investigate the prepared nano-ferrites compositions. The sintered nano-ferrites samples of Mg, Ni, Cu, Co, La, Fe and O were used for this spectroscopy to confirm their existence according to stoichiometric calculations as mentioned in Table 8 and also the chemical reaction completion. The surface defects crystalline of the prepared nanoparticles can affect the EDAX quantification, and is the reason for the difference between theoretical and observed elemental analysis [59].

Fig. 11 (a-f) shows the image of EDS spectra for samples x varies as 0.00, 0.03, 0.06, 0.09, 0.12 and 0.15.

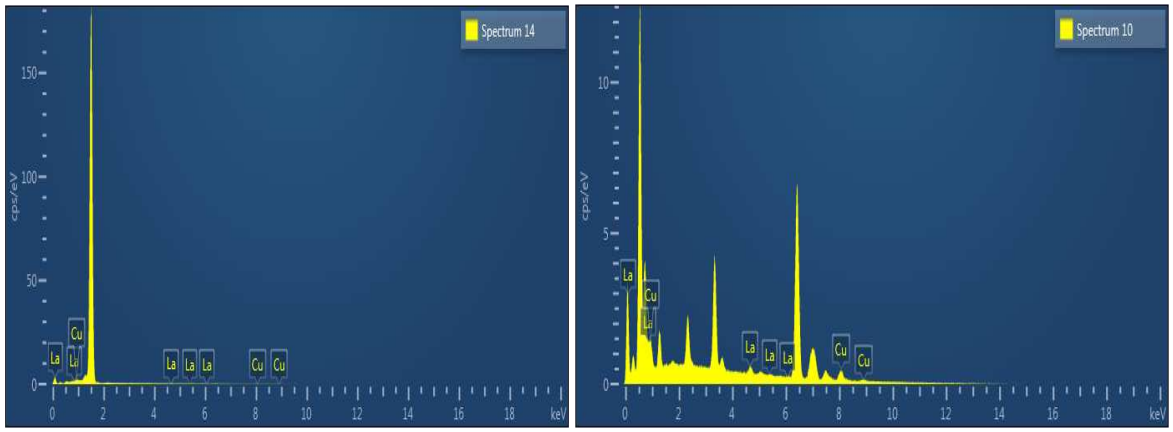

(a) x =0 (b)x =0.03

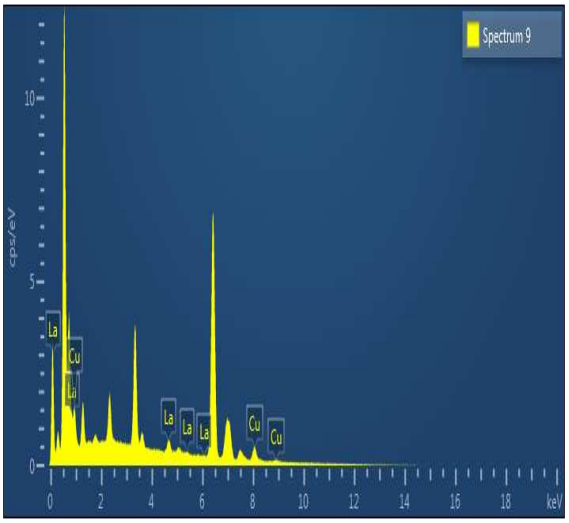

(c) x =0.06

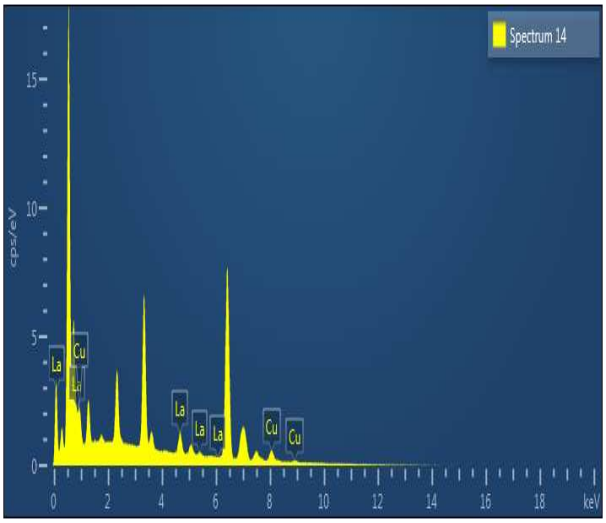

(d) x =0.09

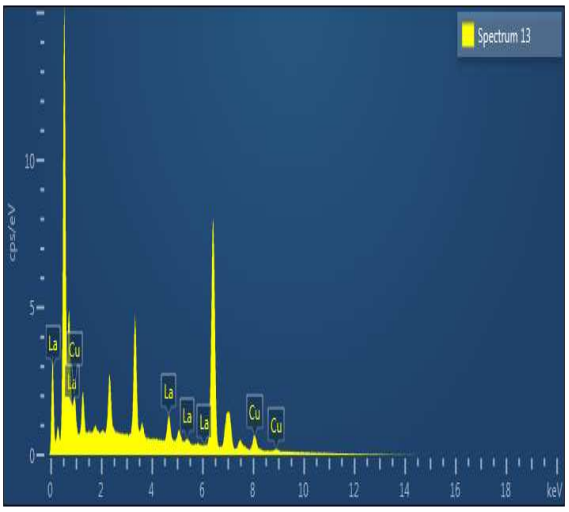

(e) x =0.12

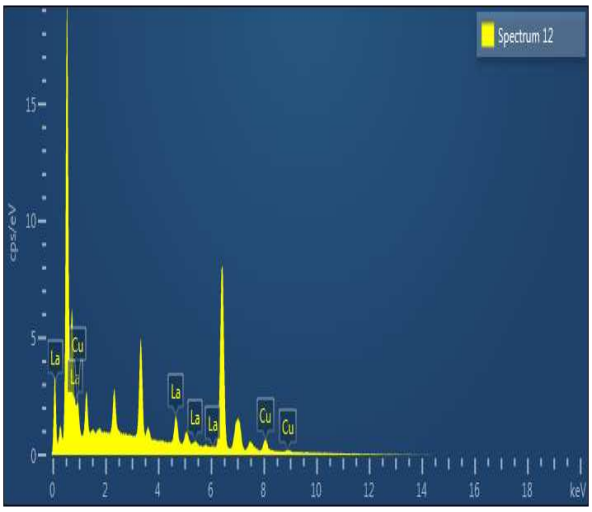

(f) x =0.15

Fig. 11: Spectrum of EDX for $Mg_{0.25}Ni_{0.15}Cu_{0.25}Co_{0.35}Fe_{2-x}La_xO_4$

Table 8: Elemental Composition of $Mg_{0.25}Ni_{0.15}Cu_{0.25}Co_{0.35}Fe_{2-x}La_xO_4$ as x varies 0.0, 0.03, 0.06, 0.09, 0.12 and 0.15

Elements	**x =0**		**x =0.03**		**x =0.06**		**x =0.09**		**x =0.12**		**x =0.15**	
	Actual	**Obsr.**	**Actual**	**Obser**	**Actual**	**Obser**	**Actual**	**Obser**	**Actua**	**Obser v**	**Actual**	**Obser v**
Mg	3.571	2.07	3.571	4.25	3.571	3.89	3.571	4.40	3.571	4.02	3.571	4.33
Ni	2.142	1.02	2.142	2.86	2.142	2.53	2.142	2.57	2.142	2.39	2.142	2.39
Cu	3.571	3.098	3.571	3.13	3.571	3.83	3.571	4.12	3.571	4.18	3.571	3.79

Co	5.00	1.29	5.00	5.23	5.00	5.60	5.00	4.91	5.00	5.13	5.00	4.56
La	0.00	0.00	0.42	0.65	0.85	0.82	1.285	1.69	1.714	1.93	2.14	2.26
Fe	28.14	35.17	28.14	35.17	27.71	35.65	27.28	30.69	26.85	34.65	26.42	30.88
O	57.14	48.71	57.14	48.71	57.14	47.16	57.14	51.63	57.14	47.70	57.14	51.77

3.8. I-V Characterizations

The electric properties of the prepared La^{3+} doped nanoparticles were investigated through the two probes method. The pellets definite dimensions were made from the hydraulic press having diameter 7 mm. Silver paste was used to connect the pellet to the probes of the IV apparatus. The graph between the current and voltage of the series $Mg_{0.25}Ni_{0.15}Cu_{0.25}Co_{0.35}Fe_{2-x}La_xO_4$ is given in Fig 12. In order to find the resistivity for all samples the following relation was used;

$$\boldsymbol{R = \frac{\rho L}{A}} \qquad (20)$$

Where, R represents the resistance of nanomaterials, L is the width of pellet and A indicates the area of pellet.

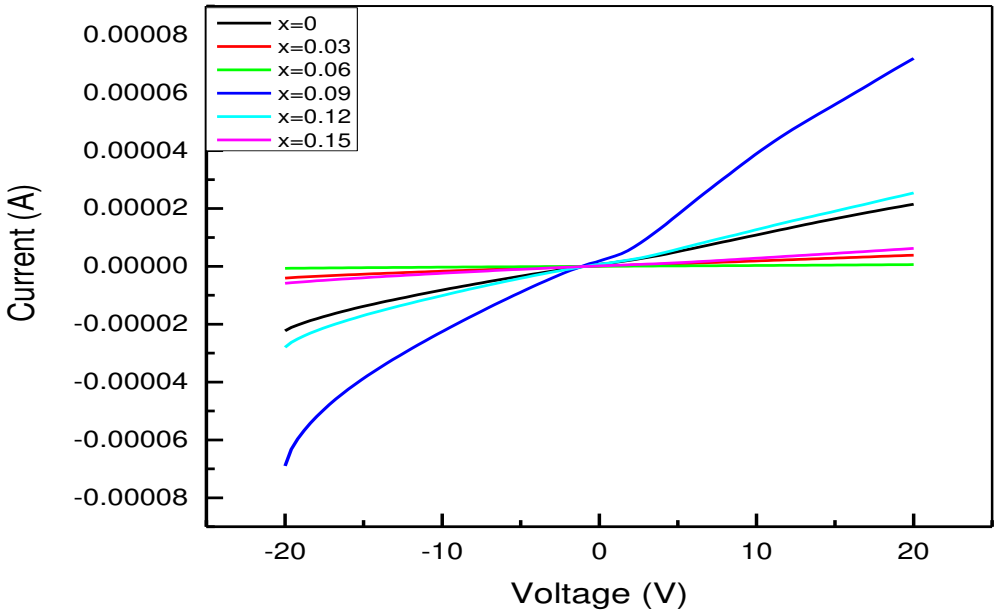

Fig. 12: I-V curves of $Mg_{0.25}Ni_{0.15}Cu_{0.25}Co_{0.35}Fe_{2-x}La_xO_4$ spinel ferrites at 50°C

The relation between resistivity and temperature of prepared La^{3+} samples is calculated with the help of given formula

$$\rho = \rho_o \exp\left(\frac{\nabla E}{k_B T}\right) \qquad (21)$$

Here ρ indicates DC electrical resistivity, ρ_o represents temperature constant, activation energy is represented by ∇E and k_B denotes Boltzmann`s constant. It is observed from the calculated data that the rise in temperature cause the decrease in the DC resistivity due to hopping of electrons to equivalent lattice sites within same element [57].

The relation between resistivity and temperature can be found out by using,

$$\rho_{DC} = \rho_o \exp\left(\frac{\nabla E}{\boldsymbol{K_B T}}\right) \qquad (22)$$

In this formula,ρ_{DC}indicates DC electrical resistivity, and ρ_o represents resistivity at infinite temperature [60].

Compositional Variation of DC Resistivity

The IV data revealed the decrease in DC resistivity due to La^{3+} ions doping in the samples. DC resistivity data reveals the exchange of electrons between $Fe^{3+} \leftrightarrow Fe^{2+}$ and also La^{3+} ions with Fe^{3+} due to La^{3+} ions doping. Figs 12 are the graphs between the log of resistivity and concentration of La^{3+} doped prepared samples. The IV data showed that the electric resistivity is minimum for x=0.09 for all temperatures and maximum when there is no doping of La^{3+} ions.

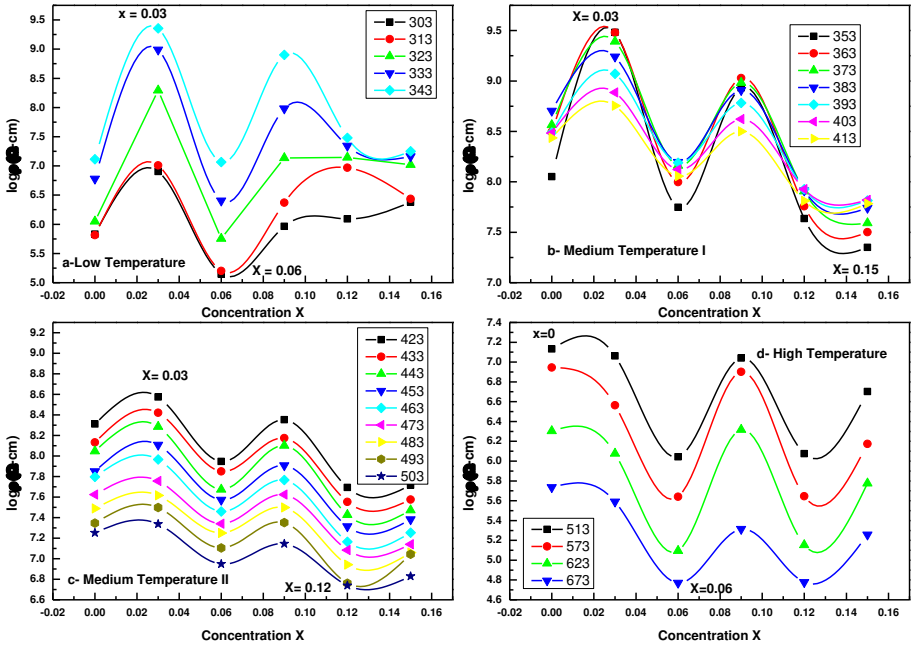

Fig. 13: Graph between log of Resistivity and Concentration (La^{3+}) of $Mg_{0.25}Ni_{0.15}Cu_{0.25}Co_{0.35}Fe_{2-x}La_xO_4$ with four zones of temperature (a) Low Temperature (303 K-343 K) (b) Medium Temperature I (353 K-413 K) (c) Medium Temperature II (423 K-503 K) (d) High Temperature (513 K-673 K)

Fig. 13(a) represents the graph between the log of resistivity and La^{3+} ions concentration at low temperature (303 K to 343 K) and shows that the highest value for the log of resistivity is the x=0.03 samples and the lowest value for the log of resistivity is for x=0.06.

Fig. 13 (b) is for the medium temperature range (353 K - 413 K) for the log of resistivity as a function of La^{3+} ions concentration. In this temperature range, the x=0.15 sample has the lowest log of resistivity and the x=0.03 sample has the highest log of resistivity value.

Fig. 13 (c) is for the medium temperature II range (423 K – 503 K) with the highest and lowest value of log of resistivity for the prepared samples at x=0.03 and x=0.12 respectively.

Fig. 13 (d) is for the high temperature range (513 K – 673 K) with the highest value of log of resistivity for x=0.00 and the lowest value of log of resistivity for x=0.06.

Fig.13 shows the decrease in log of resistivity with the addition of La^{3+} ions for the prepared samples. It also confirms the replacement of La^{3+} ions with Fe^{3+} ions at octahedral sites. As a result, it slows down the electron exchanging between Fe^{2+} and Fe^{3+} and also reduced the electron hopping. The electron hopping is the basic reason of conduction in ferrites due to existing of same element in more than one valence state that is distributed on equivalence lattice site.

Fig. 14 represents the trend in the resistivity measurements with respect to 1000/temperature. It has two regions, the first region has the temperature range of 303 K to 380 K, while the second region has the range above 380 K. Kink occurs at range (370 K - 380 K) for all the samples and called the transition and Curie temperatures. These obtained curves are divided into ferromagnetic and paramagnetic regions. The conductivity phenomenon of these prepared samples with La^{3+} ions, confirmed a significance change order in the magnetism origin. It is also confirm that the ferromagnetism region is observed before the transition temperature while the paramagnetic region is observed after the transition temperature.

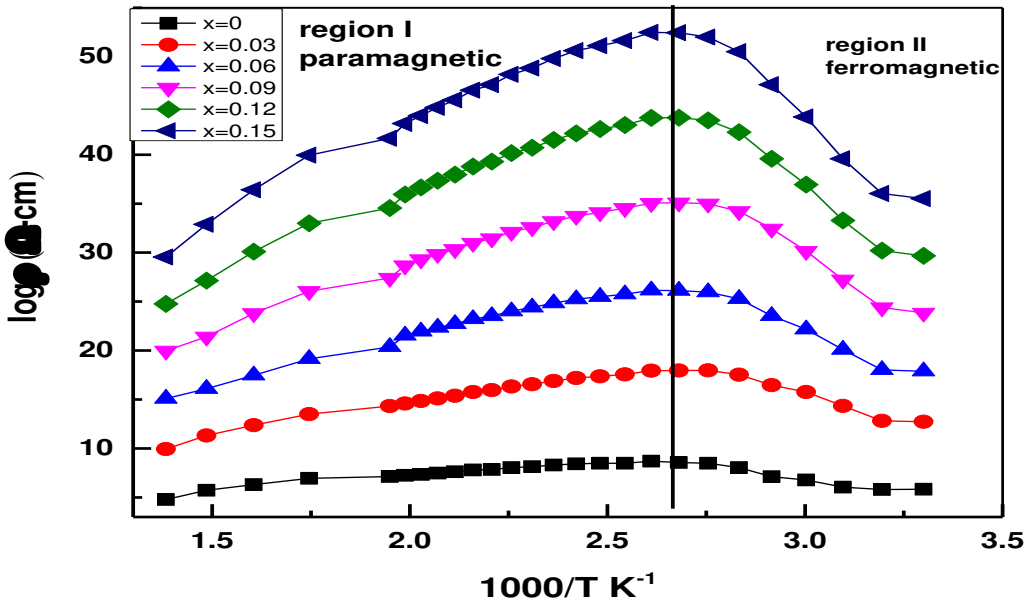

Fig. 14: Graph between log of Resistivity and 1000/ T (K^{-1}) of $Mg_{0.25}Ni_{0.15}Cu_{0.25}Co_{0.35}Fe_{2-x}La_xO_4$

The activation energy E_a, of the prepared nanoparticles is calculated using:

$$E_a = 2.303 \times k_B \times 10^3 \times \text{slope (eV)} \qquad (23)$$

Here k_B is Boltzmann constant. The activation energy ($E_a = E_p - E_f$) is calculated through the difference of activation energies from paramagnetic region (E_p) to ferromagnetic region (E_f) as represented in Fig 15 [61].Due to this reason, the activation energy firstly increased from x = 0 to 0.09 and after decreased from x = 0.09 to 0.15 that is good agreement with the reported literature [62].

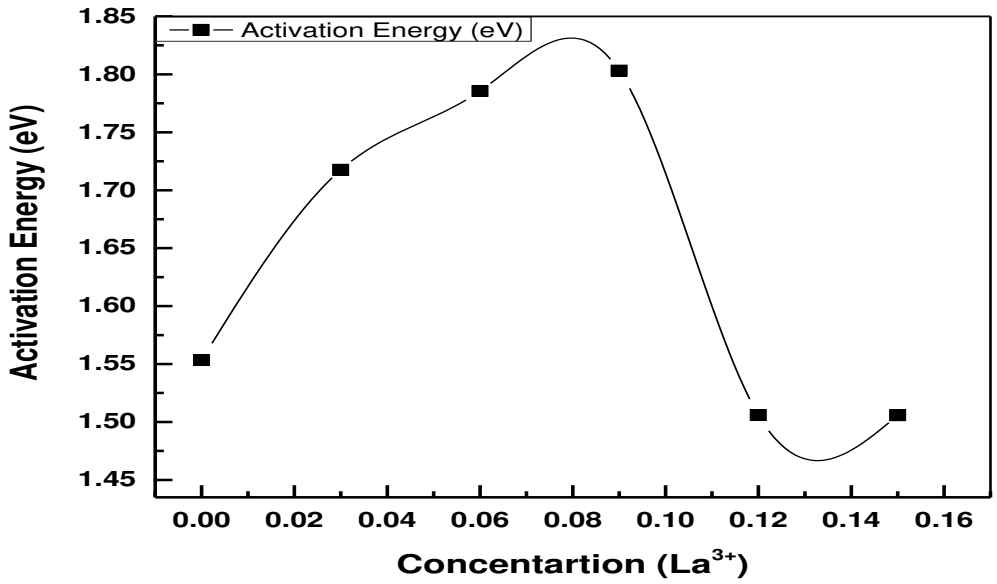

Fig. 15: Graph between activation energy and concentration (La^{3+})

The values of activation energy of $Mg_{0.25}Ni_{0.15}Cu_{0.25}Co_{0.35}Fe_{2-x}La_xO_4$ as x varies 0.00, 0.03, 0.06, 0.09, 0.12, 0.15 are given in table 9.

Table 9: Activation Energy and Curie Temperature of $Mg_{0.25}$ $Ni_{0.15}$ $Cu_{0.25}$ $Co_{0.35}$ Fe_{2-x} La_x O_4 as x varies 0.0, 0.03, 0.06, 0.09, 0.12 and 0.15.

x	Curie Temperature	DC Activation Energy (eV)		
	T_c (K)	E_p	E_f	$E_a = E_p - E_f$
0	373	0.5613	-0.9921	1.5525
0.03	371	0.6337	-1.0839	1.7176
0.06	374	0.6468	-1.0387	1.6855
0.09	380	0.5423	-1.2608	1.8031
0.12	381	0.4992	-1.0067	1.5059
0.15	382	0.5073	-0.9973	1.5046

4. Conclusion

La^{3+} doped spinel ferrites were prepared by the auto combustion sol-gel method. The cubic spinel structure was evaluated through XRD analysis and variation in the calculated lattice constants was observed due to La^{3+} ions doping. X-ray density, crystallite size and ionic radii r_A(Å) and r_B(Å) showed variation due to the addition of La^{3+}ions in to the ferrites. FTIR spectrum confirmed the preference of La^{3+} on the octahedral site as the variation in the frequency band was observed which was also confirmed from the Raman data. SEM indicated the morphological properties of the prepared samples that have uniformity in structure with the addition of La^{3+} doping and the stoichiometry composition of the prepared samples were confirmed through EDS analysis. UV-Vis data revealed a remarkable reduction in the energy band gap from 2.48 to 1.53 eV in the optical characteristics, which was also confirmed from the IV data. The activation energy bands varied from 1.803 to 1.505 eV due to the doping of La^{3+}ions into the prepared samples.

References:

1. Shinde T.J., Gadkari A.B., Vasambekar P.N. 2012. Influence of Nd^{3+} substitution on structural, electrical and magnetic properties of nanocrystal line nickel ferrites. *Journal of Alloys and Compounds*, 513: 80-85.

2. Sripriya R. C., Mahendiran M, J. Madahavan and M. Victor Antony Raj. 2019. Enhanced magnetic Properties of $MgFe_2O_4$ nanoparticles. *Science Direct Materials Today: Proceedings* 8: 310–314.

3. Ganure K.A., L.A Dhale, V. T Katkar, K. S Lohar. 2017. Synthesis and Characterization of Lanthanum-doped Ni-Co-Zn Spinel Ferrites Nanoparticles via Normal Micro-Emulsion Method. *International Journal of Nanotechnology and Applications*, 11(2): 189-195.

4. Pervaiz E., Gul I. 2013. Influence of rare earth (Gd^{3+}) on structural, gigahertz, dielectric and magnetic studies of cobalt ferrites. *Journal of Physics*: Conference Series, 439: 012015.

5. Kadam A.A., S. S. Shinde , S. P.Yadav, P .S .Patil, K. Y. Rajpure. 2013. Structural, morphological, electrical and magnetic properties of Dy doped Ni–Co substitutional spinel ferrite. *Journal of Magnetism and Magnetic Materials,* 329: 59–64.

6. Kumara K., A. Loganathan. 2018. Structural, Electrical and Magnetic Properties of Large ionic size Sr^{2+}ions Substituted Mg Ferrite Nanoparticles. *Journal of Materials Chemistry and Physics,* S0254-0584-30336-5.

7. Ahmed M. A., E. Ateia, S.I. El-Dek. 2003. Rare earth doping effect on the structural and electrical properties of Mg–Ti ferrite. *Materials Letters*, 57: 4256–4266.

8. Kanna R. R., K. Sakthipandi, S.M. Seeni Mohamed Aliar Maraikkar, N. Lenin, M. Sivabharathy. 2018. Doping effect of Rare-earth (lanthanum, neodymium and gadolinium) ions on the structural, optical, dielectric and magnetic properties of copper nanoferrites. *Journal of Rare Earths,* 36(12): 1299-1309.

9. Bharathi K. K. and C.V. Ramana. 2010. Improved electrical and dielectric properties of La-doped Co ferrite. *Journal of Materials Research Society*, 26(4): 584-591.

10. Kumar P., S. K. Sharma, M. Knobel, M. Singh. 2010. Effect of La^{3+} doping on the electric, dielectric and magnetic properties of cobalt ferrite processed by co-precipitation technique. *Journal of Alloys Compound,* 508: 115–118.

11. Indhrajothi R., I. Prakash, M. Venkateswarlu, N. Satyanarayana. 2015. Lanthanum ion (La^{3+}) substituted $CoFe_2O_4$ anode material for lithium ion battery applications. *J. Chem*. 39, 4601–4610.

12. Slimani Y., Unal B., Almessiere M. A., Korkmaz A. D., Shirsath S. E., Yasin G., A.V. Trukhanov A. V. and Baykal A. 2020. Investigation of structural and physical properties of Eu^{3+} ions substituted $Ni_{0.4}Cu_{0.2}Zn_{0.4}Fe_2O_4$ spinel ferrite nanoparticles prepared via sonochemical approach. *Results in Physics,* 17: 103061.

13. M.A. Almessiere M. A., A.D. Korkmaz A. D., Y. Slimani Y., Nawaz M., Ali S., A. Baykal A. 2019. Magneto-optical properties of Rare Earth metals substituted Co-Zn spinel nanoferrites. *Ceramics International*, 45(3): 3449-3458.

14. Almessiere M. A., Unal B., Slimania Y., Korkmaz A. D., Baykal A., I. Ercan I. 2019. Electrical properties of La^{3+} and Y^{3+} ions substituted $Ni_{0.3}Cu_{0.3}Zn_{0.4}Fe_2O_4$ nanospinel ferrites. *Result in Physics,* 15:102755.

15. Almessiere M. A., Slimani Y., Korkmaz A. D., Güner S., Baykal A., Shirsath S. E., Ercan I., Kögerler P. 2020. Sonochemical synthesis of Dy^{3+} substituted $Mn_{0.5}Zn_{0.5}Fe_{2-x}O_4$ nanoparticles: structural, magnetic and optical characterizations *Ultrasonics Sonochemistry,* 104836.

16. Sadaqata A., Almessiere M., Slimani Y., Guner S., Sertkol M., Albetran H., A. Baykal A., Shirsath S. E., Ozcelik B., Ercan I. 2019. Structural, optical and magnetic properties of Tb^{3+} substituted Co nanoferrites prepared via sonochemical approach. *Ceramics International,* 45: 22538–22546.

17. Shirsath S. E., B.G. Toksha, K. M. Jadhav. 2009. Structural and Magnetic Properties of Large ionic size In^{3+} ions Substituted $NiFe_2O_4$ Ferrite. *Journal of Materials Chemistry and Physics,* 117: 163-168.

18. Mathur P., A. Thakur, M. Singh. 2008. Low Temperature synthesis of $Mn_{0.4}Zn_{0.6}In_{0.5}Fe_{1.5}O_4$ nanoferrites for high frequency applications. *Journal Physics and Chemistry of Solids*, **69:**187-192.

19. Kale A., S. Gubbala, R. D.K. Misra, 2004. Magnetic behavior of nano-crystalline nickel ferrite synthesized by the reverse micelle technique. *Journal of Magnetism and Magnetic Materials,* **277:**350-358.

20. Hussain F. I., R. A. Najem. 2018. La^{3+} effectiveness replacement on the ferrite material

($Cu_{0.2}Zn_{0.45}La_xFe_{2-x}O_4$) on the structural and electrical and magnetic features. *Journal of Physics*. 1003: 012097.

21. Ikram S., Jacob J., Arshad M. I., Mahmood K.,Ali A., Sabir N., Amin N. and Hussain S. 2018. Tailoring the Structural, Magnetic and Dielectric properties of Ni-Zn-CdFe2O4 spinel ferrites by thesubstitution of Lanthanum ions. *Ceramics International,* S0272-8842(18)33104-3.

22. Chaudhari V., S. E. Shirsath, M. L. Mane, R. H. Kadam, S. B. Shelke, D. R. Mane. 2013. "Crystallographic, magnetic and electrical properties of $Ni_{0.5}Cu_{0.25}Zn_{0.25}La_xFe_{2-x}O_4$ nanoparticles fabricated by sol–gel method", *Journal of Alloys and Compounds,* 549:213–220.

23. Wang Y., J. Jiang, F. Xu, L. Li, H. Liu, H. Qiu, 2008, "Magnetic properties of La-substituted Ni–Zn–Cr ferrites via rheological phase synthesis"*, Material Chemistry and Physics,* 112: 769-773.

24. Zhou X., J. Jiang, L. Li, X. Feng, 2007, "Preparation and magnetic properties of La-substituted Zn–Cu–Cr ferrites via a rheological phase reaction method", *Journal of Magnetism and MagneticMaterials.* 314: 7-10.

25. Kittel, C., McEuen, P.,McEuen, P. 1996. Introduction to solid state physics (Vol. 8, pp. 323-324). New York: Wiley.

26. Schaefer, H. E., Kisker, H., Kronmüller, H., Würschum, R. 1992. Magnetic properties of nano crystalline nickel. *Nanostructured materials*, 1(6), 523-529

27. Mukhtar, A., F. Aen, M.U. Islam, S. B. Niazi, M.U. Rana. 2011. Structural, physical, magnetic and electrical properties of La-substituted W-type hexagonal ferrites. *Ceramics International,* 37: 3691–3696.

28. Ahmed, M. A., N. Okasha, M. Oaf, R.M. Kershi. 2007. The role of Mg substitution on the microstructure and magnetic properties of BaCo Zn W-type hexagonal ferrites. *Journal of Magnetism and Magnetic Materials,* 314: 128–134.

29. Iqbal, M. J., Ahmad, Z., Meydan, T., Melikhov, Y. 2012. Physical, electrical and magnetic properties of nano-sized Co-Cr substituted magnesium ferrites. *Journal of applied physics*, 111(3), 033906.

30. Prabahar, S. and Dhanam, M. 2005. CdS thin films from two different chemical baths-structural and optical analysis. *Journal of Crystal growth*, 285(1-2): 41-48.

31. Kavetskyy, T., Shpotyuk, O., Popescu, M., Lorinczi, A. and Sava, F. 2007. FSDP-related correlations in chalcogenide glasses. *Journal of optoelectronics and advanced materials*, 9(10): 3079.

32. Prasad, M. S. R., Prasad, B. B. V. S. V., Rajesh, B., Rao, K. H. and Ramesh, K. V. 2011. Magnetic properties and DC electrical resistivity studies on cadmium substituted nickel–zinc ferrite system. *Journal of Magnetism and Magnetic Materials*, 323(16): 2115-2121.

33. Prasad, B. B. V. S. V., B. R. Babu, M. S. R. Prasadi. 2015. Structural and dielectric studies of Mg^{2+} substituted Ni–Zn. *Materials Sciences,*33 (4): 806-815.

34. Zeeshan, T., S. Anjum, H. Iqbal, R. Zia. 2018. Substitutional effect of copper on the cation distribution in cobalt chromium ferrites and their structural and magnetic properties. *Journal of Materials Science*, 36(2): 255-263.

35. Jadhav, S.S., S. E. Shirsath, B. G. Toksha, S. M. Patange, S. J. Shukla and K. M. Jadhav. 2009. Structural Properties and cation distribution of Co-Zn nanoferrites. *International Journal of Modern Physics B,* 23(30): 5629–5638.

36. Mahmoud, M. H., Hamdeh, H. H., Ho, J. C., O'shea, M. J. and Walker, J. C. 2000. Mössbauer studies of manganese ferrite fine particles processed by ball-milling. *Journal of magnetism and magnetic materials,* 220: 139-146.

37. Kugimiya, K. and Steinfink, H. 1968. Influence of crystal radii and Electronegativities on the crystallization of AB_2X_4 stoichiometries. *Inorganic Chemistry*, 7(9): 1762-1770.

38. Gabal, M. A., Al Angari, Y. M. and Al-Agel, F. A. 2013. Synthesis, characterization and magnetic properties of Cr-substituted Co–Zn ferrites nanopowders. *Journal of Molecular Structure,* 1035: 341-347.

39. Hemeda, O. M., Said, M. Z. and Barakat, M. M. 2001. Spectral and transport phenomena in Ni ferrite-substituted Gd_2O_3. *Journal of magnetism and magnetic materials*, 224: 132-142

40. Gabal, M. A., A. M. Asiri, Y. M. AlAngari. 2011. On the structural and magnetic properties of La- substituted NiCuZn ferrites prepared using egg-white. *Ceramics International*, 37: 2625-2630.

41. R. D. Waldron.1995. Infrared spectra of ferrites. *Phys. Rev*. 99. 1727.

42. Kryszewski M. and Jeszka J.K.1998. Nanostructured conducting polymer composites—super paramagnetic particles in conducting polymers. *Synthetic Metals*, 94:99–104

43. Sonia, M. M. L., Blessi S., Pauline S. 2014. Effect of copper substitution on the structural, morphological and magnetic properties of nickel ferrites. *International Journal of Research* 1:1051–1054.

44: Zhang W., Sun A., Zhao X., Suo N., Yu L., Zuo Z. 2019. Structural and magnetic properties of La^{3+} ion doped Ni–Cu–Co nano ferrites prepared by sol–gel auto-combustion method. *Journal of Sol-Gel Science and Technolog,* 90: 599–610.

45. Nayakv H., Pati S.K. and Bhatta D. 2004. Decomposition of γ - irradiated $La_2(C_2O_4)_3$ + CuO mixture: a non-isothermal study. *Radiation effects and defects in solids,* 159**:** 93-106.

46. Himansulal, N. 2015. Kinetics Study on the Thermal Decomposition of Lanthanum Oxalate Catalysed by Zn-Cu Nano Ferrites. *Research Journal of Material Sciences,* 3(2), 1-8.

47. Ali, I., Ahmad M., Islam M. U., Awan M. S. 2013. Substitution effects of La^{3+} ions on the structural and magnetic properties of Co_2Y hexaferrites synthesized by sol–gel autocombustion method. *Journal of Sol-Gel Science and Technolog,* 68: 141–149.

48. G.P. Joshi, N.S. Saxena, R. Mangal, A. Mishra, T.P. Sharma. 2003. Bandgap determination of Ni–Zn ferrites. *Bull. Mater. Sci*, 26(4): 387–389.

49. Hussain K., Bibi A., Jabeen F.,Amin N., Mahmood K., Ali A., Iqbal M. Z., Arshad M. I. 2020. Study of structural, optical, electrical and magnetic properties of Cu^{2+} doped $Zn_{0.4}Co_{0.6-x}Ce_{0.1}Fe_{1.9}O_4$ spinel ferrites. *Physica B,* 584: 412078.

50. Sinha A. and Dutta A. 2020.Structural, optical and electrical transport properties of some rare-earth-doped nickel ferrites. *Journal of Physics and Chemistry of Solids*, 145: 109534.

51. Shebanova, O. N. and P. 2003. Lzaor. Raman Spectroscopic study of magnetite ($FeFe_2O_4$). *Journal of Solid State Chemistry*, 174: 424-430.

52. Nandan, B., M. C. Bhatnagar and S. C. Kashyap. 2019. Cation distribution in nanocrystalline cobalt substituted nickel ferrites: X-ray diffraction and Raman Spectroscopic investigation. *Journal of Physics and Chemistry of Solids*, 129: 298-306.

53. Wu, Y., T. Yao, Y. Lu, B. Zou, X. Mao, F. Huang, H. Sun, X. Chen. 2017. Magnetic, Dielectric and magnetodielectric properties of Bi-layered perovskite $Bi_{4.25}Gd_{0.75}Fe_{0.5}Co_{0.5}Ti_3O_{15}$. *Journal of Material Sciences*, 52: 1-9.

54. Liu, S., K. Wei, Y. Cheng, S. Yan, L. He and L. Deng. 2019. Structural, magnetic and microwave electromagnetic properties in La- Substituted quaternary ferrite. *Journal of Alloys and Compounds*, 791: 469-476.

55. Akhtar, M. N., A. B. Sulong and M. A. Khan. 2018. Systematic study of Ce^{3+} on the structural and magnetic properties of Cu nanosized ferrites for potential applications. *Journal of Rare Earth,* 36: 156-164.

56. Noorkhan P. A. and S. Kalayne. 2012. Synthesis, Characterization Ac Conductivity of Nickel Ferrite. *Journal of Engineering Research and Applications*, 2 (4): 681-685.

57. Mullai, R. U., P. P. Pradeep, G. Chandrasekaran. 2012. Synthesis and characterization of Lanthanum doped Mg-Zn Ferrite Nanoparticles Prepared by sol-Gel Method. *Journal of Recent Trends in Science and Technology*, 5: 78-85.

58. Ketan A. Ganure, Laxman A. Dhale, Sagar E. Shirsat, Kishan S. Lohar. 2018. Morphological Study of Lanthanum Doped Nano Spinel Ferrite via Normal Micelles Method. *Journal of Inorganic and Organometallic Polymers and Materials*, 10904-018-0825-8.

59. K.S. Lohar, S.M. Patange, M.L. Mane, S.E. Shirsath, Cationic Distribution investigation and characterization of $Ni_{1-x}Cd_x$ Fe_2O_4 nanoparticles synthesized by citrate gel process. *Journal of Mol. Struct.* 1032, 105-110 (2013).

60. Anantharaman, M. R., Jagatheesan, S., Malini, K. A., Sindhu, S., Narayanasamy, A., Chinnasamy, C. N. and Brongersma, H. H. 1998. On the magnetic properties of ultra-fine zinc ferrites. *Journal of magnetism and magnetic materials,* 189(1): 83-88.

61. Amin N., Hasan M. S., Majeed Z., Latif Z., Nabi M. A., Mahmood K., Ali A., Mehmood K., Fatima M., Akhtar M., Akhtar M. I., Bibi A., Iqbal M. Z., Jabeen F and Bano N. 2020. Structural, electrical, optical and dielectric properties of yttrium substituted cadmium ferrites prepared by Co-Precipitation method. *Ceramics International*, https://doi.org/10.1016/j.ceramint.2020.05.079

62. Hasan M. S., M. I. Arshad, A. Ali, K. Mahmood, N. Amin, S. S. Ali, M. I. Khan, G. Mustafa, M. J. Khan and M. Saleem. 2019. Mg and La co-doped ZnNi spinel ferrites for low resistive applications.*Materials Research Express,* 6: 016302.